Self-Assembly and Molecular Dynamics of Peptide-Functionalized Polyphenylene Dendrimers

M. Mondeshki, G. Mihov, R. Graf, H. W. Spiess, and K. Müllen

Max-Planck-Institut für Polymerforschung, D-55021 Mainz, Germany

P. Papadopoulos, A. Gitsas, and G. Floudas*

University of Ioannina, Department of Physics, P.O. Box 1186, 451 10 Ioannina, Greece, and Foundation for Research and Technology-Hellas (FORTH), Biomedical Research Institute (BRI)

Received September 13, 2006; Revised Manuscript Received November 1, 2006

ABSTRACT: The self-assembly mechanism and the associated molecular dynamics are studied for a series of poly-L-lysine-functionalized polyphenylene dendrimer melts as a function of the core size (generation), functionality, and polypeptide length using X-rays, solid-state NMR, calorimetry, and dielectric spectroscopy. A striking dependence of the polyphenylene self-assembly on the poly-L-lysine length is shown. In addition, the type (α-helix/β-sheet) of peptide secondary structure is controlled by the packing restrictions imposed by the polyphenylene core. We show that constrained poly-L-lysines can adopt different secondary structures from their linear analogues. The dynamic investigation revealed significant mobility associated solely with the polypeptide through three processes: a glass transition, a slower process associated with the relaxation of α-helical segments, and a glassy mode whose origin could be resolved by site-specific solid-state NMR techniques. Solid-state NMR studies further indicated a mobility gradient in going from the rigid peptide backbone to the side chains.

I. Introduction

Drug delivery systems such as lipid- or polymer-based nanoparticles can be designed to improve the pharmacological and therapeutic properties of drugs. Advancement of polymer chemistry has led to nanoscale construction capabilities with potential in designing novel drug delivery systems.[1,2] Dendrimer chemistry is considered a pioneering tool for such applications because it offers ideal dimensions, monodispersity, solubility, biocompatibility, and unique spherical shape that, in addition, is highly functionalizable.[3−6]

Recently, the synthesis and conformation of dendronized polymers based on a poly-L-lysine backbone[7] as well as the synthesis of L-lysine dendronized polystyrene[8] has been reported. Dendrimers based on poly-L-lysines have attracted interest for the possible development of multiple antigen peptides or as nonviral gene delivery systems.[9,10] An interesting finding in the study of dendronized polymers based on the poly-L-lysine backbone with attached polyester dendrons was the observation of a transition from a compact α-helical backbone to a disordered yet extended conformation with increase in dendron size.[7] Steric repulsions between the dendrons were thought to be responsible for the observed helix-to-coil transition.

Recent progress in this direction has been the development of synthetic routes leading to peptide functionalization of polyphenylene dendrimers.[11,12] These molecules are monodisperse and shape persistent, with topologically isolated, noninteracting functional groups that are employed as scaffolds for the attachment of poly-L-lysines, giving rise to core−shell nanostructured materials. In addition, polyphenylene dendrimers bearing the fluorescent perylenediimide core provide the possibility of optical detection of the dendritic conjugates.

In the present study, we employ a series of poly-L-lysine-functionalized polyphenylene dendrimer melts[12] with different polyphenylene core sizes, functionality, and peptide degree of polymerization (of the type $G_gF_fN_n$, where G, F, and N stands for the generation, functionality, and peptide degree of polymerization, respectively, with values in the range: $1 \leq g \leq 2$, $4 \leq f \leq 16$, and $9 \leq n \leq 84$ (Table 1 and Figure 1)), and report a striking dependence of the conjugates' self-assembly on the length of the polypeptide that is independent of the polyphenylene generation. Our results are compared with model linear poly-L-lysine compounds (**Plys$_{20}$** and **Plys$_{59}$**). By using X-ray scattering and solid-state NMR, we show that poly-L-lysines can adopt a different secondary structure as compared to their linear analogues when attached to polyphenylene cores. In addition, by combining dielectric spectroscopy with site-specific solid-state NMR heteronuclear recoupling techniques, we are able to follow the polypeptide and polyphenylene dynamics and identify the mobile sites and the associated dynamic order parameters.

Table 1. Molecular Characteristics of the Peptide-Functionalized Polyphenylene Dendrimers

sample	generation	X	$n_{Lys,UV}$[a]	$n_{Lys,GPC}$[b]	M_w/M_n[c]
$G_1F_4N_{14}$	1	H	9	14	1.11
$G_1F_4N_{54}$	1	H	50	54	1.16
$G_1F_4N_{84}$	1	H	85	84	1.15
$G_1F_8N_{12}$	1	R	9	12	1.09
$G_1F_8N_{60}$	1	R	68	60	1.08
$G_1F_8N_{74}$	1	R	76	74	1.10
$G_2F_8N_9$	2	H	6	9	1.17
$G_2F_8N_{22}$	2	H	28	22	1.42
$G_2F_8N_{37}$	2	H	41	37	1.27
$G_2F_{16}N_{16}$	2	R	14	16	1.26
$G_2F_{16}N_{58}$	2	R	41	58	1.50
$G_2F_{16}N_{68}$	2	R	89	68	1.42

[a] Number of peptide residues per chain obtained from UV. [b] Number of peptide residues per chain obtained from GPC. [c] Polydispersity of the peptide−dendrimer conjugates calculated from gel permeation chromatography, obtained in DMF against polystyrene standards.

II. Experimental Section

Samples. The detailed synthesis of the poly-L-lysine-functionalized polyphenylene dendrimers has been described previously.[12] The poly-L-lysine chains were grafted directly from the surface of

* Corresponding author. E-mail: gfloudas@cc.uoi.gr.

10.1021/ma0621270 CCC: $33.50
Published on Web 12/06/2006

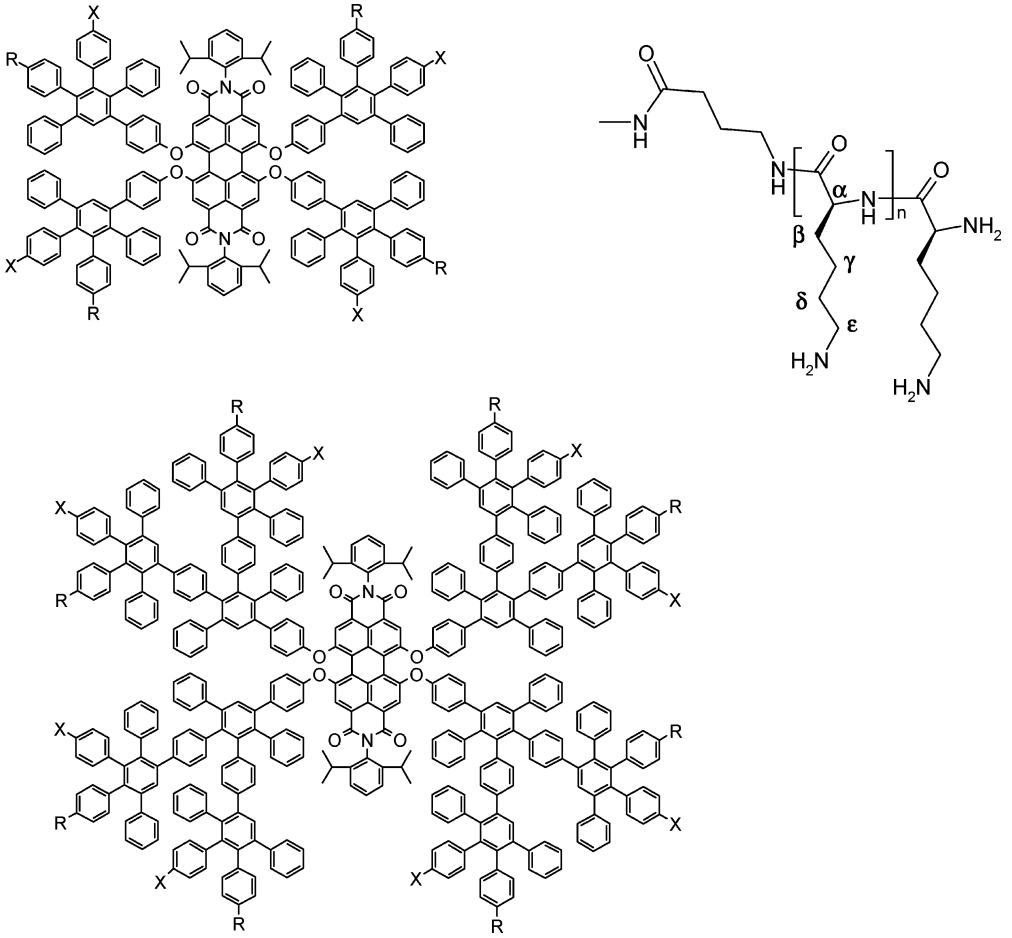

Figure 1. Polyphenylene scaffold of dendrimers of the first (top) and second (bottom) generation. X is either H or R. The repeat unit of lysine R is also shown together with the assignment of the different carbons.

first- and second-generation amino-functionalized polyphenylene dendrimers (PPD) consisting of pentaphenylbenzene units and a rigid perylenediimide core. By applying this dendrimer type[11] as macroinitiator of polymerization, it allows one to place a certain number of functional groups into a defined volume element and even to control their orientation.[13−15] The grafting of poly-L-lysine from the surface of PPD was achieved via ring-opening polymerization of ϵ-benzyloxycarbonyl-L-lysine−*N*-carboxy-anhydride (Lys(Z)−NCA). This reaction scheme permits control of the polypeptide length via the amount of Lys(Z)−NCA added to the reaction. The grafting was followed by deprotection of the lysine ϵ-amino groups. The resulting polypeptide−PPD conjugates possess different numbers of poly-L-lysine chains of variable length, as shown in Figure 1 and Table 1. The molecular characteristics of the polyphenylene dendrimers of the $G_gF_fN_n$ type, (G, F, and N stands for the generation, functionality, and peptide degree of polymerization, respectively) are given in Table 1.

Thermal properties: Differential Scanning Calorimetry (DSC). A Mettler Toledo star differential scanning calorimeter (DSC) was used for the thermal analysis. The poly-L-lysine-functionalized polyphenylene dendrimers were first heated at a rate of 10 K/min to 423 K and subsequently cooled to 153 K with 10 K/min. A second heating run, with the same rate, was used to identify the glass transition temperature, T_g, the width of the transition, ΔT_g, and the step in the specific heat capacity, Δc_P. Figure 2 gives the DSC traces from two conjugates of the first (**$G_1F_8N_{60}$**) and second (**$G_2F_{16}N_{68}$**) generation. Both traces show the step-like change in the specific heat associated with the peptide glass transition.[16]

Solid-State NMR. NMR experiments were performed on a Bruker Avance spectrometer with a ^{1}H Larmor frequency of 700.13 MHz and a ^{13}C frequency of 176.05 MHz. A Bruker double resonance probe, supporting rotors of 2.5 mm outer diameter at a spinning frequency of 30 kHz, was used for all experiments. At high spinning frequencies, heating effects caused by air friction become significant. The effective sample temperature, ~323 K, has been corrected for these friction effects following the known procedure.[17] For all NMR experiments, the length of a 90° ^{1}H pulse was 2.5 μs, and recycle delays of 2 s were used. For ^{13}C cross-polarization (CP)/magic-angle spinning (MAS) NMR experiments, 2−4 k transients were recorded with a duration of the variable amplitude (80−100%) CP contact pulse of 1 ms, and the two-pulse

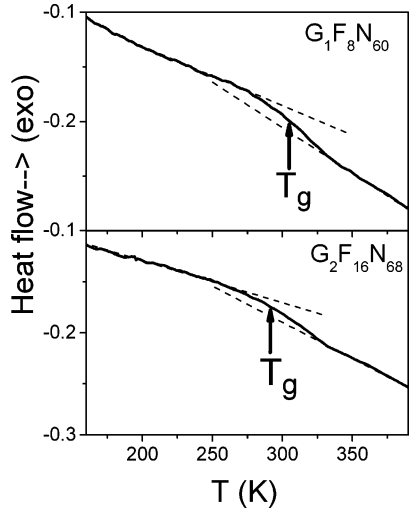

Figure 2. DSC traces obtained during the second heating run (rate 10 K/min) from two poly-L-lysine-functionalized polyphenylene dendrimers of the first (**$G_1F_8N_{60}$**) (top) and second (**$G_2F_{16}N_{68}$**) (bottom) generation. The arrows indicate the corresponding glass temperatures.

Table 2. Secondary Structures of the Poly-L-lysine-Functionalized Polyphenylene Dendrimers, as Determined by WAXS and Solid-State NMR[a]

		secondary structure		aromatic core	peptide backbone	peptide side groups[c] (C_β, $C\gamma$, C_δ CH_2)		($C\epsilon CH_2$)	
sample	n	NMR	WAXS	order parameter S	order parameter S	order parameter S	excursion angle (deg)	order parameter S	excursion angle (deg)
$G_2F_8N_9$	9	dis[b]		0.95		0.67	20	0.45	30
$G_1F_8N_{12}$	12								
$G_1F_4N_{14}$	14	dis[b]		~1	0.95	0.69	18	0.55	25
$G_2F_{16}N_{16}$	16	α	α (hcp)	0.90	0.95	0.67	20	0.60	23
$G_2F_8N_{22}$	22	α	α (hcp)	~1	0.95	0.50	27	0.50	27
$G_2F_8N_{37}$	37	α	α (hcp)	~1	0.95	0.53	26	0.35	41
$G_1F_4N_{54}$	54	α/β (3/1)	α (hcp)	~1	0.95	0.48	29	0.30	45
$G_2F_{16}N_{58}$	58	β/α (2/1)		~1	0.95	0.50	27	0.50	27
$G_2F_{16}N_{68}$	68	α/β (1/1)							
$G_1F_8N_{74}$	74		α (hcp)						
$G_1F_4N_{84}$	84	β/α (1/1)		~1	0.95	0.55	25	0.50	27
$Plys_{20}$	20	β							
$Plys_{59}$	59	α/β (1/1)							

[a] The local dynamic order parameters of the aromatic core, the peptide backbone, and the side groups are presented together with the mean excursion angles,[20] characteristic for each individual segment in the course of its motion. [b] Disordered state with ill-defined secondary structures. [c] A gradient of mobility along the peptide side groups from the rigid core toward the side chain ends is found for most of the compounds, studied by solid-state NMR. The presented local order parameters and the related excursion angles are an average of the site-specific S values and excursion angles of the C_β, C_γ, and C_δ methylene groups (see Figure 1). The terminal $C_\epsilon CH_2$ group, being the most mobile, is discussed separately.

phase-modulation (TPPM) heteronuclear decoupling scheme was applied during the acquisition of the ^{13}C signal.[18] In the $^{13}C-^{1}H$ rotor-encoded rotational-echo double resonance (REREDOR) experiment,[19] the initial proton magnetization was transferred to carbons following the CP-MAS protocol. Subsequently, $^{13}C-^{1}H$ dipolar couplings were recoupled by applying two blocks of π-pulse trains, consisting of 6 π pulses with $\tau_R/2$ spacing each, where τ_R is the rotor period of the MAS. The recoupling blocks were spaced by a time interval t_1, which was incremented in 20 steps from 0 to τ_R in order to monitor the rotor-encoding of the recoupling scheme. By Fourier-transforming the modulated ^{13}C signal intensity, sideband patterns were obtained that reflect the $^{13}C-^{1}H$ dipolar couplings. The coupling of a ^{13}C spin to more than one ^{1}H spin is represented by the product:

$$S \propto \langle \prod_i \cos(N_{exc}\bar{\Phi}_0^{(i)} - \Phi^{(i)}(0;t_1) - N_{rec}\bar{\Phi}_{t_1}^{(i)} + \Phi^{(i)}(t_1;2t_1)) \rangle \quad (1)$$

where the brackets denote the powder average and N_{exc} and N_{rec} the number of rotor periods used for excitation and reconversion, respectively, while the time evolution is acquired as a sum of the phases resulting from the action of the REREDOR sequence. The two terms $\Phi^{(i)}(0;t_1)$ and $\Phi^{(i)}(t_1;t_2)$ are the phases acquired due to the residual dipolar evolution during the intervals t_1 and $2t_1$. In the conditions of very fast magic-angle spinning or weak dipole−dipole couplings, these terms become small, or even negligible, compared to the recoupling terms $N_{exc}\bar{\Phi}_0^{(i)}$ and $N_{rec}\bar{\Phi}_{t_1}^{(i)}$ in eq 1. The reduction of the dipole−dipole coupling of selected spin pairs is specified by local dynamic parameters, S, which are defined as the ratio of the measured effective $^{13}C-^{1}H$ couplings to their hypothetical values for a totally rigid pair, i.e., $0 \le S \le 1$. The results of the solid-state NMR dynamics[20] and conformational studies are summarized in Table 2.

X-ray Scattering. Both wide-angle and small-angle X-ray scattering (WAXS and SAXS) measurements have been performed. For the WAXS measurements, a Siemens $\theta-\theta$ diffractometer (model D500T) was used in reflection geometry. The Cu Kα radiation was used from a Siemens generator (Kristalloflex 710 H) operating at 35 kV and 30 mA, and a graphite monochromator was utilized in front of the detector ($\lambda = 0.154$ nm). Measurements were made in the 2θ range from 0.1 to 40° in steps of 0.01°. The following thermal history was employed: First, the samples were heated to 393 K and subsequently slowly cooled to 303 K. Diffractograms were taken at 393, 373, 333, 313, and 303 K for all samples. Additional WAXS measurements were made from macroscopically oriented (extruded) filaments (at $T = 423$ K) with a diameter of 0.7 mm using a pinhole collimation and a two-dimensional detector (Siemens A102647) with 1024 × 1024 pixels. A graphite monochromator was used ($\lambda = 0.154$ nm), and the sample-to-detector distance was 7.2 cm. SAXS measurements were made at the X27C beamline at Brookhaven National Laboratory. The wavelength was 0.1371 nm, and the sample-to-detector distance was at 2.173 m. Measurements were made at different temperatures: 393, 363, 333, and 303 K.

Dielectric Spectroscopy (DS). The dielectric measurements were performed at different temperatures in the range 123−473 K, at atmospheric pressure, and for frequencies in the range from 10^{-2} to 10^{6} Hz using a Novocontrol BDS system composed of a frequency response analyzer (Solartron Schlumberger FRA 1260) and a broadband dielectric converter. The sample cell consisted of two electrodes 20 mm in diameter and the sample with a thickness of 55 μm. The complex dielectric permittivity $\epsilon^* = \epsilon' - i\epsilon''$, where ϵ' is the real and ϵ'' is the imaginary part, is generally a function of frequency ω, temperature T, and pressure P, although here only the frequency and temperature dependencies have been investigated.[21] The analysis has been made using the empirical equation of Havriliak and Negami:[22]

$$\frac{\epsilon^*(\omega,T) - \epsilon_\infty(T)}{\Delta\epsilon(T)} = \frac{1}{[1 + (i\omega\tau_{HN}(T))^{\alpha}]^{\gamma}} \quad (2)$$

where $\Delta\epsilon(T)$ is the relaxation strength of the process under investigation, τ_{HN} is the relaxation time of the equation and α, γ ($0 < \alpha$, $\alpha\gamma \le 1$) describe the symmetrical and asymmetrical broadening of the distribution of relaxation times, and ϵ_∞ is the dielectric permittivity at the limit of high frequencies. The relaxation times at maximum loss (τ_{max}) are presented herein and have been analytically obtained by the Havriliak−Negami equation as follows:

$$\tau_{max} = \tau_{HN}\left[\frac{\sin\left(\frac{\pi\alpha}{2(1+\gamma)}\right)}{\sin\left(\frac{\pi\alpha\gamma}{2(1+\gamma)}\right)}\right]^{-1/\alpha} \quad (3)$$

At lower frequencies, ϵ'' rises due to the conductivity ($\epsilon'' = \sigma/(\omega\epsilon_f)$, where σ is the dc conductivity, and ϵ_f the permittivity of free space. The conductivity contribution has also been taken into account during the fitting process. The measured ϵ'' spectra have been used for the analysis except at high temperatures, where the derivative of ϵ' has been employed ($d\epsilon'/d \ln \omega \sim -(2/\pi)\epsilon''$). Because ϵ' is not affected by the conductivity, this method is very useful in fitting relaxation processes that are hidden under the conductivity, provided that the system is free of surface polarization

effects. Therefore, the latter representation was employed in the analysis of the slower process.

In a second approach, we used the electric modulus representation:[21,23]

$$M^* = \frac{1}{\epsilon^*} = M' + iM'' \tag{4}$$

This representation is very sensitive to the presence of slow processes (see below) and to the process due to ionic mobility. The relaxation times corresponding to the M'' maximum are close to the ones from the ϵ'' and are related through $\tau_{M''} = \tau_{\epsilon''}(1 + \Delta\epsilon/\epsilon_\infty)^{-1/\alpha}$ in the case of a symmetric distribution ($\gamma = 1$).

III. Results and Discussion

Self-Assembly in the Melt State. It is now well-established that the ^{13}C chemical shifts are sensitive probes of the peptide local conformation, and thus the ^{13}C cross-polarization/magic-angle spinning (CP-MAS) solid-state NMR technique has been widely employed in identifying the predominant polypeptide secondary structures (α-helices and β-sheets).[24,25] The observed differences in chemical shifts of the secondary structures arise from variations of the dihedral angles (Φ and Ψ) depending on the local conformation of individual amino acid residues and is correlated with the type of hydrogen bonding (i.e., intra- or intermolecular). Figure 3 gives some representative spectra of a model linear poly-L-lysine with 20 residues (**Plys$_{20}$**) and two of the poly-L-lysine-functionalized polyphenylene dendrimers of the second generation with 16 (**G$_2$F$_{16}$N$_{16}$**) and 58 (**G$_2$F$_{16}$N$_{58}$**) amino acid residues, respectively, recorded at 323 K. In the **Plys$_{20}$** spectrum, the strong signals with chemical shifts at 172 and 53 ppm arise from the amide C═O and the C_α carbon, respectively, and indicate the formation of β-sheets. In contrast, a longer linear poly-L-lysine with 59 residues (**Plys$_{59}$**) (not shown) displays two amide C═O resonances at 176 and 171.5 ppm as well as two C_α resonances at 58 and 53, with relative intensities suggesting a 1:2 α-helix to β-sheet ratio. Interestingly, in the conjugate **G$_2$F$_{16}$N$_{16}$**, the single C═O and C_α resonances are at 176 and 58, respectively, revealing a predominant α-helical secondary structure in contrast to **Plys$_{20}$**. In fact, the α-helical secondary structure dominates the peptide conformations for the poly-L-lysine-functionalized polyphenylene dendrimers with intermediate degrees of polymerization ($16 \leq n \leq 37$) independent of generation and functionality. Peptide-functionalized polyphenylene dendrimers with the shorter peptides ($n \leq 14$) do not clearly prefer either of the two secondary structures, but the overall chemical shift is closer to that of the β-sheet structure. Presumably, these oligopeptides are too short to stabilize a proper secondary structure. For the longer poly-L-lysines, $n \geq 54$, a mixture of both conformations is formed as revealed by the spectrum of **G$_2$F$_{16}$N$_{58}$** in Figure 3. We mention here that X-ray studies on protonated poly-L-lysines in aqueous solutions demonstrated the possibility of an α-helix to β-sheet transition at high relative humidity.[26] The results for the secondary structures determined for all samples are summarized in Table 2. These results suggest an effect of the polyphenylene core on the peptide secondary conformation. This is especially the case for the poly-L-lysine-functionalized polyphenylene dendrimers with intermediate degrees of polymerization that form predominantly α-helices in contrast to their linear counterparts. Below, we will explore the reason for this effect by using X-ray scattering at the appropriate length scales (see below).

Small-angle X-ray scattering of the conjugates revealed a broad peak with corresponding distances that reflect polyphenylene core-to-core correlations. The intensity and sharpness of the peak is a function of the number of poly-L-lysine residues; the shorter the poly-L-lysine, the better resolved the SAXS peak. This is shown in Figure 4 for the G_1F_8 series as a function of poly-L-lysine length (n = 12, 60, and 74, respectively, for **G$_1$F$_8$N$_{12}$**, **G$_1$F$_8$N$_{60}$**, and **G$_1$F$_8$N$_{74}$**). The broad peak at $q \sim 1.15$ nm^{-1} in **G$_1$F$_8$N$_{12}$** results in a characteristic distance of 6.7 nm (assuming only nearest neighbor correlations, i.e., $l = 1.23 \times 2\pi/q$). This distance is a function of the polyphenylene generation, thus clearly reflecting correlations between the polyphenylene cores. These correlations become very weak for the longer poly-L-lysines, as shown by the absence of this peak for **G$_1$F$_8$N$_{60}$** and **G$_1$F$_8$N$_{74}$** in the SAXS patterns of Figure 4.

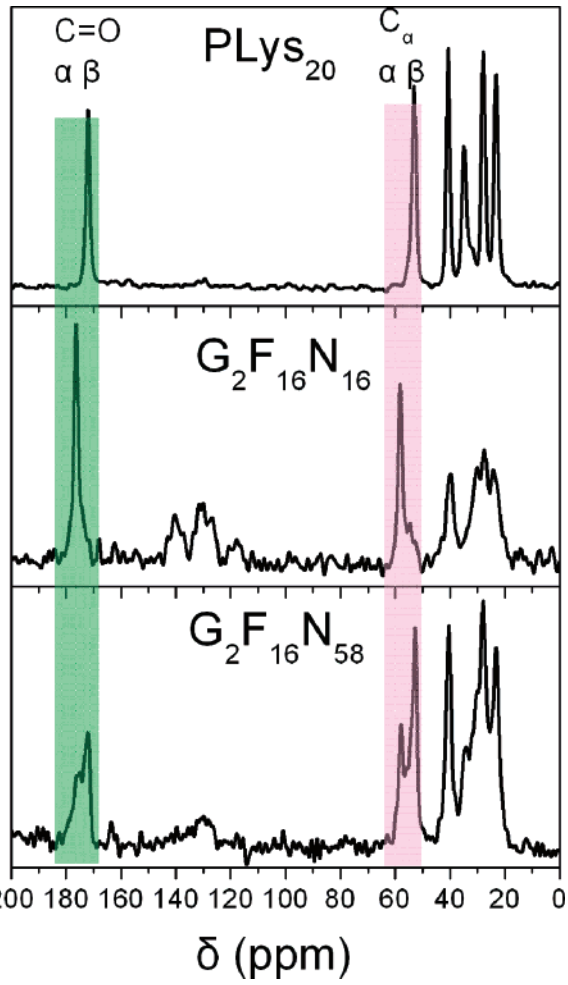

Figure 3. ^{13}C CP NMR spectra, recorded at 30 kHz MAS and 1 ms cross-polarization time, of a linear poly-L-lysine (**Plys$_{20}$**) and two of the poly-L-lysine-functionalized polyphenylene dendrimers with n = 16 (**G$_2$F$_{16}$N$_{16}$**) and n = 58 (**G$_2$F$_{16}$N$_{58}$**). The C_α ($\delta \sim 53-58$ ppm) and amide C═O ($\delta \sim 172-176$ ppm) resonances suggest that **Plys$_{20}$** has solely the β-sheet form, whereas the peptide-functionalized polyphenylene dendrimers form predominantly α-helices (**G$_2$F$_{16}$N$_{16}$**) or a mixture of β-sheets and α-helices (**G$_2$F$_{16}$N$_{58}$**). The solid-state NMR results on the peptide secondary structures of the series are summarized in Table 2.

WAXS was employed for two reasons: first, to identify the peptide conformation in the conjugates in comparison to the NMR results and second, to estimate their lateral coherence (packing efficiency). With respect to the type of secondary structure, the WAXS images from extruded fibers (Figure 5) revealed hexagonally packed α-helical structures for the peptide-substituted polyphenylenes dendrimers with the longer poly-L-lysines. As an example, in Figure 5, the two-dimensional image and the total integrated intensity from **G$_1$F$_8$N$_{74}$** (n = 74) is

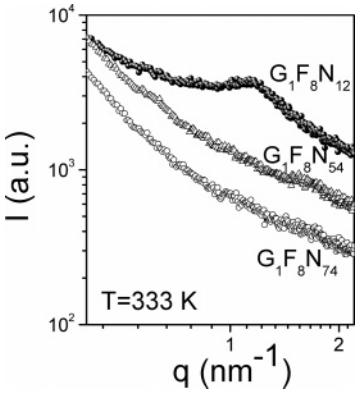

Figure 4. SAXS curves from three first-generation peptide-functionalized polyphenylene dendrimers as a function of the poly-L-lysine degree of polymerization: $n = 12$ (**$G_1F_8N_{12}$**), $n = 60$ (**$G_1F_8N_{54}$**), and $n = 74$ (**$G_1F_8N_{74}$**). Notice the broad peak at $q \sim 1.15$ nm^{-1} (with corresponding distances at $l \sim 6.7$ nm) that is absent in the dendrimers with the longer poly-L-lysines.

shown. The integrated intensity profile contains strong equatorial reflections at relative positions $1:3^{1/2}:4^{1/2}$, suggesting hexagonally packed α-helices and a broader reflection with a corresponding spacing of ~0.5 nm originating from interatomic distances. The type of secondary structure is generally in good agreement with the NMR results (Table 2). In addition to the type of the peptide secondary structure, the WAXS images revealed a correlation between the poly-L-lysine length and their lateral packing efficiency; the WAXS patterns exhibit sharp reflections associated with the lateral spacing of α-helixes only for the longer poly-L-lysines (as in Figure 5 right, for the G_2F_8 series), and the longer the poly-L-lysine, the better resolved the hexagonal reflections of α-helices. This suggests a coupling between the longer-range core-to-core correlations (SAXS), with the shorter range correlations originating from the packing of α-helices (WAXS). For the peptide-substituted polyphenylenes dendrimers with the short polypeptide chains ($n < 16$), the secondary structure is ill-defined, consisting mostly of random conformations as well as some extended conformations and α-helices (as determined by solid-state NMR) attached to the polyphenylene cores. The latter possess some correlations between their centers and give rise to the SAXS peak. These oligolysines exhibit only weak lateral correlations within their secondary structures, as shown by the very weak WAXS reflections (Figure 5). In contrast, the substituted polyphenylene dendrimers with the longer polypeptides ($n > 20$) lack correlations among their polyphenylene cores but do show improved lateral correlations between their secondary structures that assemble into hexagonally packed α-helices (Figure 5). This situation in the poly-L-lysine-substituted polyphenylene dendrimers is depicted in a schematic way in Figure 6. The figure depicts core-to-core correlations for the shorter polylysines that are absent in the longer ones. In the latter case, however, the α-helices self-assemble into a hexagonal lattice. Notice that the α-helices are shown as "broken" for reasons that will become clear below.

Dynamics in the Liquid State. Studying the poly-L-lysine-substituted polyphenylene dendrimers with dielectric spectroscopy can provide not only the dynamics but also can clarify the morphology picture. DS is very sensitive to the presence of the liquid-to-glass transition and to secondary relaxations below the "glass temperature" T_g and to slower modes originating from the relaxation of the peptide secondary structures. The origin of the dynamic arrest of protein dynamics at T_g has been a point of interest.[23,27−30] Recent investigations[27,28] have shed some light onto this problem by following the freezing of the dynamics at the liquid-to-glass transition in a series of oligopeptides of γ-benzyl-L-glutamate up to the polymer (PBLG), and in poly(*Z*-L-lysine) (PZLL) and poly(*p*-benzyl-L-tyrosine) (PTyr) using dielectric spectroscopy as a function of temperature and pressure. This process, in the different polypeptides, is the typical α process found in amorphous polymers and glass-forming liquids

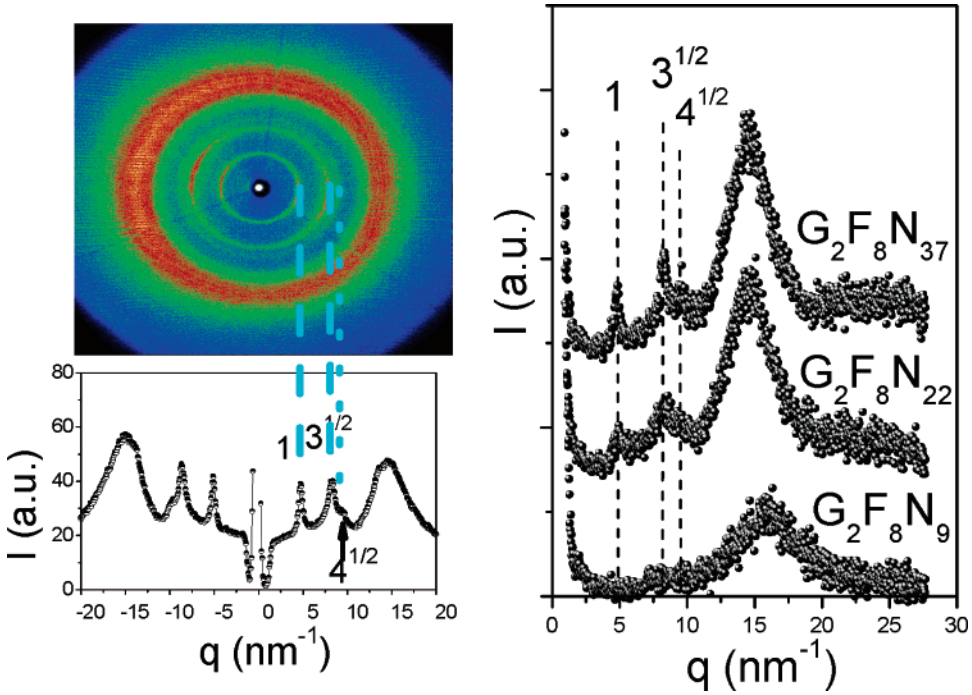

Figure 5. (Left) Two-dimensional wide-angle X-ray diffraction pattern from an oriented **$G_1F_8N_{74}$** fiber (extruded at 423 K and measured at 303 K). The total integrated intensity profile obtained from the 2-D pattern is shown together with the positions of the most intense reflections with relative positions at $1:3^{1/2}:4^{1/2}$, suggesting hexagonally packed poly-L-lysine α-helices. (Right) Dependence of the WAXS reflections (obtained with a $\theta-\theta$ diffractometer) on the poly-L-lysine degree of polymerization. The G_2F_8 series is shown with $n = 9$ (**$G_2F_8N_9$**), $n = 22$ (**$G_2F_8N_{22}$**), and $n = 37$ (**$G_2F_8N_{37}$**) at 303 K. Notice the intense reflections with relative positions at $1:3^{1/2}:4^{1/2}$ for the longer poly-L-lysines.

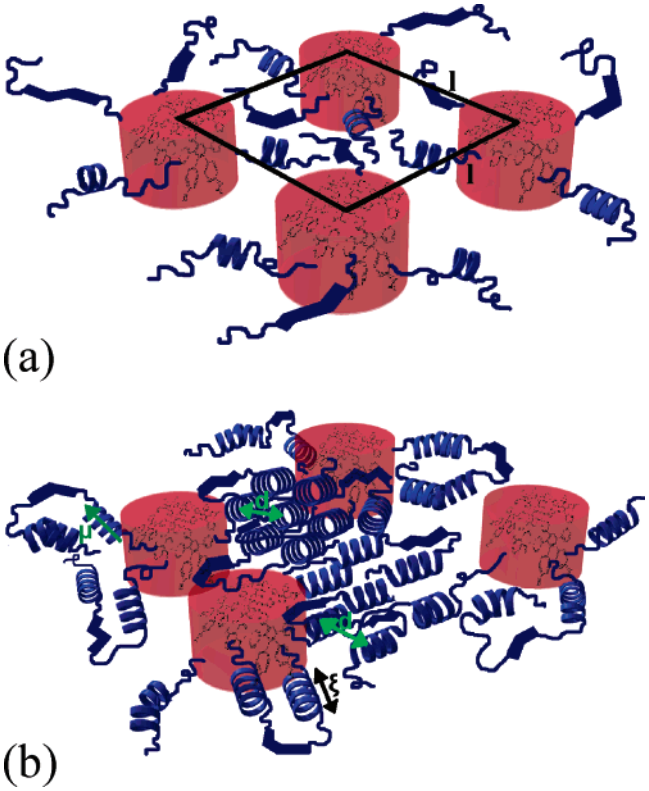

Figure 6. Schematic representation of the self-assembly in the functionalized polyphenylene dendrimers with (a) short polypeptides ($n < 16$) and (b) longer polypeptides ($n > 20$). Notice in the former the absence of a well-defined secondary peptide structure and that the polyphenylene dendrimers forming the core have some degree of order as revealed from SAXS. In the latter, the α-helical secondary structure prevails (with persistence length ξ) that, in addition, display packing in a hexagonal lattice (with a distance d) (WAXS). Notice the absence of correlations between the cores in this case.

associated with the glass-to-liquid relaxation of amorphous segments.[27] This assignment was based on (i) the existence of a step in the specific heat, Δc_P, (ii) the strong temperature dependence of the relaxation times $\tau(T)$, (iii) the broad and T-dependent distribution of relaxation times, (iv) the molecular weight dependence of the dynamic T_g,[28] and (v) the pressure dependence. With respect to the latter, two of us have shown that temperature is the controlling parameter of the dynamics associated with the α-process through the breaking/weakening of hydrogen bonds within the chain and at the chain ends (i.e., at "defects"). Furthermore, we were able to separate the solvent from the polypeptide α-process in polypeptide solutions.[31] From the above, we conclude that the liquid-to-glass "transition" in polypeptides does not relate to the solvent, but is an intrinsic feature of peptide dynamics, irrespective of the type of amino acid and of the peptide secondary structure.

In Figure 7, we show superpositions of the real and imaginary parts of the conductivity σ^*, the electric modulus M^*, and the dielectric permittivity ϵ^* for the linear **Plys$_{59}$** and the poly-L-lysine-substituted polyphenylene dendrimer **G$_2$F$_{16}$N$_{58}$** ($n = 58$) with comparable degrees of polymerization. The three representations are complementary. The electric modulus representation provides the α-process at higher frequencies and the ionic mobility, from the crossing of the real and imaginary parts, at lower frequencies/high temperatures. The dielectric permittivity representation provides the α-process as well as a slower process (this is better seen in the derivative method) associated with the relaxation of the peptide secondary structure (see below). The conductivity representation, on the other hand, emphasizes the charge carrier motion at low and high frequencies, although at higher frequencies, the charge carrier motion is coupled to molecular degrees of freedom. It is worth noticing the distinctly different spectra for the linear and poly-L-lysine-substituted polyphenylene dendrimer in Figure 7. The well-resolved α-process in **Plys$_{59}$** has moved to lower frequencies in **G$_2$F$_{16}$N$_{58}$**, whereas the slower process associated with the relaxation of the α-helical secondary structure has moved to higher frequencies.

The relaxation times associated with the segmental (α-) process of some polylysine dendrimers with comparable degrees of polymerization are shown together with the linear **Plys$_{59}$** in the usual Arrhenius representation in Figure 8. The α-process relaxation times for **Plys$_{59}$** display the usual strong non-Arrhenius T-dependence that conforms to the Vogel−Fulcher−Tammann (VFT) equation

$$\tau_{max} = \tau_0 \exp\frac{D_T T_0}{T - T_0} \tag{5}$$

where D_T is a dimensionless parameter ($= 6.0 \pm 0.5$) and T_0 (241 ± 2 K) is the "ideal" glass temperature. The usual operational definition of T_g (at $\tau \sim 10^2$ s) is in good agreement with the DSC T_g (Figure 2). The α-process in the poly-L-lysine-functionalized polyphenylene dendrimers is (i) shifted to lower frequencies/higher temperatures and (ii) displays a weaker T-dependence (with $D_T = 15$, 19, and 32 for the **G$_1$F$_4$N$_{54}$**, **G$_1$F$_8$N$_{60}$**, and **G$_2$F$_{16}$N$_{58}$**, respectively). Thus the main effect of the relatively rigid polyphenylene core on the dynamics is to slow down the segmental process. We will return to this point later with respect to the NMR results.

It is well-known that the existence of α-helical secondary structures in helical-forming polypeptides gives rise to a large dipole moment parallel to the helical axis (typical type-A polymer in Stockmayer's classification).[32] Therefore, DS has been employed both in solution and in the melt to study the dynamics of the secondary structure in PBLG. The solution studies[33,34] were able to identify the large dipole moment per peptide residue (3.4 D) and the exact molecular weight dependence ($\tau \sim M^3$) of the relaxation times. Despite these successes in understanding the dynamics of peptide α-helices, there exist theoretical and experimental results in favor of flexibility of PBLG in solution[35] and in the bulk.[28] The molecular weight dependence of the PBLG rms radius of gyration in helicogenic solvents indicated some deviations from the expected perfect helix at low and high molecular weights that could be accounted for by assuming some flexibility and randomness of the chain ends for the lower molecular weights.[35] Similarly, our recent work[28] on undiluted PBLG as a function of molecular weight revealed that both the relaxation times and the associated dielectric strength of the slower process were only weakly dependent on molecular weight, suggesting another origin for the slower process than a mere end-to-end relaxation. On the basis of these findings, two of us recently proposed a model[23] that is based on "defected" or "broken" helices that provides an estimate of the persistence length ξ from the dielectric strength of the slow process. For this purpose, the effective dipole moment was calculated from the dielectric strength of the slower process using the Buckingham equation (modified by Applequist and Mahr) suitable for rigid-rod molecules[36]

$$\frac{Nfg\mu^2}{3\epsilon_0 k_B T} = \frac{(2\epsilon_s + 1)(\epsilon_s - n^2)}{2\epsilon_s + n^2} - \frac{(2\epsilon_\infty + 1)(\epsilon_\infty - n^2)}{2\epsilon_\infty + n^2} \tag{6}$$

where N is the number density, μ is the dipole moment, f and

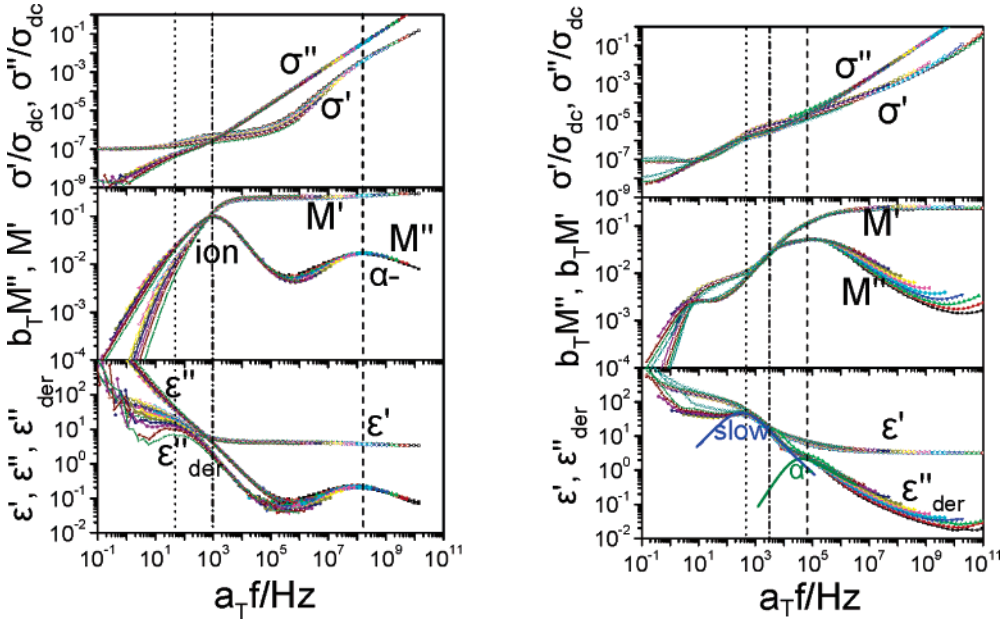

Figure 7. Superpositions of the real and imaginary parts of the conductivity $\sigma^* = i\omega\epsilon_0\epsilon^*$, the electric modulus M*, and the complex dielectric permittivity ϵ^* for **PLys$_{59}$** (left) and **G$_2$F$_{16}$N$_{58}$** (right) at a reference temperature of 413 K. The superimposed data sets are taken in 5 K increments within the temperature ranges 318−413 K and 293−413 K for **Plys$_{59}$** and **G$_2$F$_{16}$N$_{58}$**, respectively. The dashed lines give the position of the α-process M'' maximum. The dash−dotted lines give the process due to the ionic mobility and the dotted line gives the approximate position of the "slow" process (better seen in the derivate ϵ''_{der} associated with the relaxation of the peptide secondary structure).

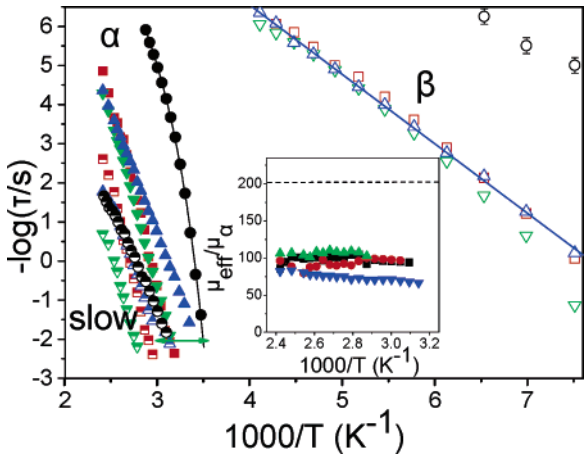

Figure 8. Arrhenius relaxation map of the different dynamic processes in the linear **Plys$_{59}$** homopolymer (circles) and three of the poly-L-lysine-functionalized polyphenylene dendrimers with similar degrees of polymerization: (squares) **G$_1$F$_4$N$_{54}$** (n = 54), (down triangles) **G$_1$F$_8$N$_{60}$** (n = 60), and (up triangles) **G$_2$F$_{16}$N$_{58}$** (n = 58). The local β-process, the segmental α-process associated with the liquid-to-glass transition, and the slow process associated with the relaxation of the secondary structure are shown with open, filled, and half-filled symbols, respectively. The lines are representative fits to the α- and β-processes using, respectively, the VFT and Arrhenius equations. The horizontal arrow gives the ΔT_g of **G$_1$F$_8$N$_{60}$**. In the inset, the normalized effective dipole moments of the same systems are shown, extracted from the slower DS process and compared with a perfectly α-helical polypeptide (dashed line) with n = 60.

g are factors related to the geometry of the molecule ($f \rightarrow {}^2/_3$ and $g \rightarrow 1$ for an infinitely long rod), ϵ_s is the static dielectric permittivity, and n is the refractive index. Thus the effective dipole moment μ_{eff} $(= g^*\mu^2)^{1/2}$, where g^* is the Kirkwood−Fröhlich pair correlation factor between neighboring dipoles was calculated for the α- and the slower process and their ratio is plotted in the inset to Figure 8 for three of the poly-L-lysine-functionalized polyphenylene dendrimers and the linear **Plys$_{59}$** as a function of temperature. The dashed line in the same figure is the expected dipole moment for a purely α-helical polypeptide (3.4 D per residue) with n = 60. Notice that the experimental points are located well below the theoretical limit for a perfect α-helix. It is for this reason that the α-helices are shown as "broken" or "defected" in the schematic representation of Figure 6. It is worth noticing that chain folding of α-helices has also been found in single crystals of poly-L-lysine.[26]

Glassy State Dynamics. At lower temperatures, another process is dielectrically active both in the linear poly-L-lysines and in the conjugates with the Arrhenius temperature dependence

$$\tau_{max} = \tau_0 \exp\left(\frac{E}{kT}\right) \tag{7}$$

where $\tau_0 \sim 10^{-14}$ s and E is the apparent activation energy ($\sim$ 35 ± 1 kJ/mol) that is practically the same in all poly-L-lysine-functionalized polyphenylene dendrimers. However, this β-process in the conjugates is several orders of magnitude slower than the corresponding process in the linear poly-L-lysine, suggesting again a large effect of chain topology on the polypeptide glassy state dynamics. Because longer-range motions are frozen in the glassy state, local dynamic processes have been studied using advanced solid-state NMR methods. In particular, techniques based on heteronuclear spin coherences, such as the rotor-encoded rotational-echo double resonance (REREDOR) or recoupled polarization transfer heteronuclear dipolar order rotor-encoding (REPT-HDOR),[37] can be used to determine the effective $^{13}C-^{1}H$ dipolar couplings via the analysis of spinning sideband patterns observed at the ^{13}C chemical shift of the CH_n group. The chemical selectivity of ^{13}C NMR spectra allows the assigning of dynamic processes to specific molecular sites and helps in elucidating the molecular origin of these dynamic processes. The dipolar coupling constant for two nuclear spins i and j spaced by an internuclear distance of r_{ij} is

$$D_{ij} \sim \frac{1}{r_{ij}^3}\cdot\frac{1}{2}(3\cos^2\theta_{ij} - 1) \tag{8}$$

where θ_{ij} is the angle of the internuclear tensor r_{ij} with respect

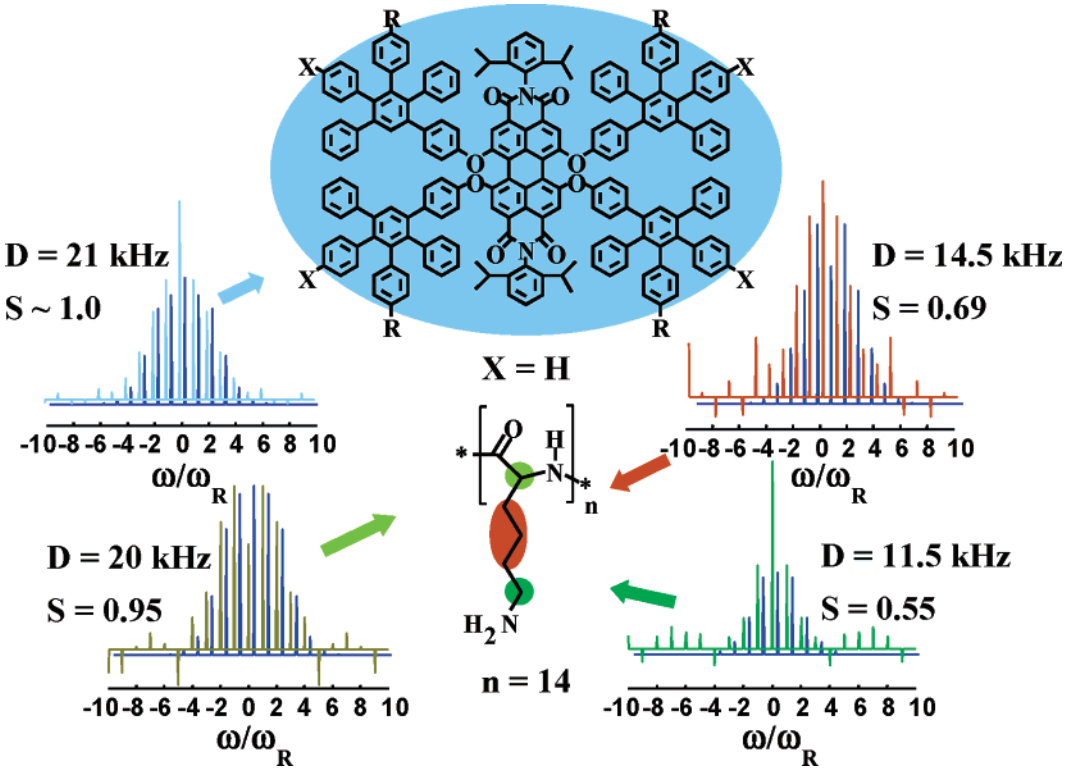

Figure 9. REREDOR sideband patterns recorded at 30 kHz MAS, 67.2 μs recoupling time, and 323 K effective sample temperature for compound $\mathbf{G_1F_4N_{14}}$, with the simulated patterns (blue) superimposed. The effective ^{1}H−^{13}C dipolar coupling constants, together with the related local dynamic order parameters, *S*, for the phenyl rings, the peptide backbone, and the peptide side groups are summarized in Table 2. These results suggest a practically frozen polyphenylene core and a mobility gradient in going from the relatively immobile peptide backbone to the side chains.

to the external magnetic field. From the dipolar coupling constant, a local dynamic order parameter S_{ij} can be defined that is independent of the internuclear distances of the coupled spins as the ratio of the motionally averaged dipole−dipole couplings and that of the rigid group:

$$S_{ij} = \left\langle \frac{1}{2}(3\cos^2\theta_{ij}(t) - 1) \right\rangle_t = \frac{\langle D_{ij}(t)\rangle_t}{D_{ij,\text{static}}} \qquad (9)$$

For fast isotropic reorientational motions, the dynamic order parameter vanishes because the effective dipolar coupling, D_{ij}, is averaged to zero, whereas for uniaxial rotations, S_{ij} depends on the angle between the internuclear tensor with the rotation axis through the second Legendre polynomial of eq 8.

The solid-state NMR ^{13}C−^{1}H REREDOR recoupling technique was used to record spinning sideband patterns for most of the poly-L-lysine-functionalized polyphenylene dendrimers under investigation. From these patterns, the effective ^{13}C−^{1}H dipolar couplings were derived and the associated local dynamic order parameters, *S*, were determined and the results are summarized in Table 2. As an example, we show in Figure 9 the recorded spinning sideband patterns together with the computed patterns for compound $\mathbf{G_1F_4N_{14}}$ ($n = 14$). The number and intensity of these spinning sideband patterns originates from the ratio of the dipolar coupling constant and the magic-angle spinning frequency. In general, the bigger the intensity of higher-order sidebands, in comparison to the central band, the stronger the dipolar couplings and the associated local dynamic order parameters.

The results presented in Table 2 reveal that, on the time scale of the NMR experiment (30 kHz, i.e., $\tau \sim 10^{-5}$ s at 323 K), the polyphenylene core, as well as the peptide backbone, are essentially frozen (typically $S \sim 0.9-1$), whereas the poly-L-lysine side groups are generally characterized by a gradient of mobility from the rigid backbone toward the more mobile end CH_2 groups (the *S* values of the side groups presented in Table 2 are an average of the local dynamic order parameters of the C_β, C_γ, and C_δ CH_2 moieties, while the *S* values of the C_ϵ CH_2 groups are reported separately). As expected, the highest residual anisotropy of the recoupled dipolar ^{13}C−^{1}H interaction is observed for the C_β CH_2 moieties (adjacent to the polypeptide backbone), where the lower degree of motional freedom gives rise to a higher local dynamic order parameter. The dipolar coupling constants gradually decreased toward the C_ϵ CH_2 groups, as the values determined for the side chain CH_2 moieties were in the range $D_{CH_2} = 11.5-14$ kHz ($S = 0.5-0.7$) for the different poly-L-lysine-functionalized polyphenylene dendrimers. Despite being in the solid state, the methylene groups show considerable mobility, reaching dynamic order parameter values of $S = 0.3-0.6$ for the C_ϵ CH_2. The observed difference (depending on the degree of polymerization and number of functionalities of the respective derivatives) of approximately 6 kHz in the dipole−dipole coupling constants of the C_ϵ CH_2 moieties indicates small differences in the local packing.

In addition, the dynamic order parameter values, as described in detail elsewhere,[20,38] can be rationalized in terms of mean excursion angles that the respective group explores during its motion. The excursion angles for C_β, C_γ, and C_δ CH_2 (as an average) and C_ϵ CH_2 groups (Figure 1) are also given in Table 2. On the basis of these mean excursion angles, it is possible to estimate the space volume that the side CH_2 groups occupy in the course of their motion. For simplicity, motion within a cone is considered,[38] and additional local fluctuations leading to further motional averaging of the dipolar couplings are ignored. Furthermore, the side group dynamics seem to be independent of the poly-L-lysine molecular weight and type of secondary structure. Thus, the dielectrically active β-process can be assigned to dipolar relaxation of the NH and CO backbone

dipoles sampled by the relaxation of the intermediate CH backbone bond together with the relaxation of the end NH_2 group. As the poly-L-lysine backbone is relatively immobile, the β-process originates mainly from the mobile side groups.

IV. Conclusions

The study of the solid-state morphology and the associated dynamics in a series of poly-L-lysine-functionalized polyphenylene dendrimers as a function of the polyphenylene core size, functionality, and peptide degree of polymerization revealed several unanticipated findings: (1) The self-assembly mechanism is governed by correlations between the polyphenylene cores and between the α-helical poly-L-lysines for the shorter and longer oligopeptide chains, respectively. Therefore the predominant factor controlling the self-assembly is the polypeptide length. (2) These packing requirements have consequences on the peptide secondary structures: poly-L-lysine-substituted polyphenylenes with $n < 16$ form ill-defined secondary structures, intermediate poly-L-lysines stabilize predominantly α-helical structures in contrast to their linear analogues, and longer poly-L-lysines ($n \geq 54$) display mixed secondary structures. Thus constrained poly-L-lysines of intermediate length can adopt secondary structures that differ from their linear analogues. This fact is of particular importance in the design of multiple antigen peptides, where knowledge of the peptide secondary structure is essential.[5] (3) The parallel investigation of the molecular dynamics revealed three processes associated with the glassy state, the liquid-to-glass transition, and the relaxation of the α-helical peptide secondary structure. Analytically, (i) the existence of a "glass transition" was identified from the step in the specific heat and from the associated $\tau(T)$ dependence of the dielectric relaxation times. This process is strongly retarded in the poly-L-lysine-functionalized polyphenylene dendrimers as compared to linear poly-L-lysines. (ii) The α-helical structures were defected, as revealed by the characteristics of the slower DS process associated with the relaxation of the secondary structure. (iii) The heteronuclear recoupling REREDOR NMR technique enabled the identification of the site-specific geometry of the motion associated with the glassy DS process as well as of the dynamic order parameters for the C−H bonds on the polyphenylenes, the peptide backbone, and side groups. These results revealed a practically frozen polyphenylene core, on the time scale of the NMR experiment, and a mobility gradient in going from the rigid peptide backbone to the peptide side groups.

Acknowledgment. We thank Dr. Ingo Schnell for insightful comments and discussions at the initial stages of this project as well as Michael Bach for help during the X-ray experiments. Financial support by the Greek GSRT (PENED 529 and 856) and by the DFG (SFB 625) is gratefully acknowledged.

References and Notes

(1) Duncan, R. *Nat. Rev. Drug Discovery* **2003**, *2*, 347.
(2) Allen, T. M.; Cullis, P. R. *Science* **2004**, *303*, 1818.
(3) Bosman, A. W.; Janssen, H. M.; Meijer, E. W. *Chem. Rev.* **1999**, *99*, 1665.
(4) Fréchet, J. M. J.; Hawker, C. J. In *Comprehensive Polymer Science*; Aggarwal, S. L., Russo, S. S., Eds.; Pergamon Press: Oxford, 1996.
(5) Stiriba, S. E.; Frey, H.; Haag, R. *Angew. Chem., Int. Ed.* **2002**, *41*, 1329.
(6) Veprek, P.; Jezek, J. *J. Peptide Sci.* **1999**, *5*, 203.
(7) Lee, C. C.; Fréchet, J. M. J. *Macromolecules* **2006**, *39*, 476.
(8) Lübbert, A.; Nguyen, T. Q.; Sun, F.; Sheiko, S. S.; Klok, H.-A. *Macromolecules* **2005**, *38*, 2064.
(9) Choi, J. S.; Joo, D. K.; Kim, C. H.; Kim, K.; Park, J. S. *J. Am. Chem. Soc.* **2000**, *122*, 474.
(10) Ohsaki, M.; Okuda, T.; Wada, A.; Hirayama, T.; Niidome, T.; Aoyagi, H. *Bioconjugate Chem.* **2002**, *13*, 510.
(11) Wiesler, U. M.; Weil, T.; Muellen, K. *Top. Curr. Chem.* **2001**, *212*, 1.
(12) Mihov, G.; Grebel-Koehler, D.; Lübbert, A.; Vandermeulen, G. W. M.; Herrmann, A.; Klok, H.-A.; Müllen, K. *Bioconjugate Chem.* **2005**, *16*, 283.
(13) Weil, T.; Wiesler, U. M.; Herrmann, A.; Bauer, R.; Hofkens, J.; De, Schryver, F. C.; Müllen, K. *J. Am. Chem. Soc.* **2001**, *123*, 8101.
(14) Mihov, G. Scheppelmann, I. Müllen, K. *J. Org. Chem.* **2004**, *69*, 8029.
(15) Bernhard, S.; Baumgarten, M.; Müllen, K. *Eur. J. Org. Chem*. **2006**, 2523.
(16) Floudas, G.; Papadopoulos, P.; Klok, H.-A.; Vandermeulen, G. W. M.; Rodriguez-Hernandez, J. *Macromolecules* **2003**, *36*, 3673.
(17) Langer, B.; Schnell, I.; Spiess, H. W.; Grimmer, A.-R. *J. Magn. Res.* **1999**, *138*, 182.
(18) Bennett, A. E.; Rienstra, C. M.; Auger, M.; Lakshmi, K. V.; Griffin, R. G. *J. Chem. Phys.* **1995**, *103*, 6951
(19) Saalwächter, K.; Schnell, I. *Solid State Nucl. Magn. Res.* **2002**, *22*, 154.
(20) Schmidt-Rohr, K.; Spiess, H. W. *Multidimensional Solid-State NMR and Polymers*; Academic Press: New York, 1994; pp 364−366.
(21) *Broadband Dielectric Spectroscopy*; Kremer, F., Schönhals, A., Eds.; Springer: Berlin, 2002.
(22) Havriliak, S.; Negami, S. *Polymer* **1967**, *8*, 161.
(23) Papadopoulos, P.; Floudas, G. *Dielectrics Newsletter*, November 2005.
(24) Kricheldorf, H. R.; Müller, D. *Macromolecules* **1983**, *16*, 615
(25) Shoji, A.; Ozaki, T.; Saito, H.; Tabeta, R.; Ando, I. *Macromolecules* **1984**, *17*, 1472
(26) Padden, F. J.; Keith, H. D.; Giannoni, G. *Biopolymers* **1969**, *7*, 793.
(27) Papadopoulos, P.; Floudas, G.; Schnell, I.; Klok, H.-A., Aliferis, T.; Iatrou, H.; Hadjichristidis, N. *J. Chem. Phys.* **2005**, *122*, 224906.
(28) Papadopoulos, P.; Floudas, G.; Klok, H. A.; Schnell, I.; Pakula, T. *Biomacromolecules* **2004**, *5*, 81.
(29) Papadopoulos, P.; Floudas, G.; Schnell, I.; Aliferis, T.; Iatrou, H.; Hadjichristidis, N. *Biomacromolecules* **2005**, *6*, 2352.
(30) Papadopoulos, P.; Floudas, G.; Schnell, I.; Lieberwirth, I.; Nguyen, T. Q.; Klok, H.-A. *Biomacromolecules* **2006**, *7*, 618.
(31) Papadopoulos, P.; Floudas, G. to be published.
(32) Stockmayer, W. H. *Pure Appl. Chem.* **1967**, *15*, 539.
(33) Wada, A. *J. Chem. Phys*. **1958**, *29*, 674; **1959**, *30*, 328; **1959**, *30*, 329.
(34) Moscicki, K.; Williams, G. *J. Polym. Sci., Polym. Phys. Ed.* **1983**, *21*, 197.
(35) Muroga, Y.; Nagasawa, M. *Biopolymers* **1998**, *45*, 281.
(36) Buckingham, A. D. *Aust. J. Chem.* **1953**, *6*, 323.
(37) Saalwächter, K.; Graf, R.; Spiess, H. W. *J. Magn. Reson.* **1999**, *140*, 471.
(38) Rapp, A.; Schnell, I.; Sebastiani, D.; Brown, S.; Percec, V.; Spiess, H. W. *J Am. Chem. Soc.* **2003**, *125*, 13284.

MA0621270